International Journal of Steel Structures
September 2011, Vol 11, No 3, 351-366
DOI 10.1007/s13296-011-3010-2

International Journal of
STEEL
STRUCTURES
www.springer.com/journal/13296

Fracture Prediction of Welded Steel Connections Using Traditional Fracture Mechanics and Calibrated Micromechanics Based Models

Yuanqing Wang*, Hui Zhou, Yongjiu Shi, and Jun Xiong

Key Laboratory of Civil Engineering Safety and Durability of China Education Ministry, Department of Civil Engineering, Tsinghua University, Beijing, 100084, China

Abstract

Fracture resistance is of primary concern in the seismic design of beam-to-column connections in steel moment resisting frames (SMRFs). Micromechanics based fracture models such as the void growth model (VGM) and the stress modified critical strain (SMCS) model provide alternative approaches for ductile fracture prediction by relating micro-mechanisms of void nucleation, growth and coalescence to macroscopic stresses and strains. In this study, the VGM and SMCS models were calibrated for Q345 structural steel and the corresponding weld, through smooth notched tensile (SNT) tests and complementary continuum finite element models (FEMs). A series of seven local connections representing beam-to-column connections in SMRFs were tested under monotonic tensile loading and the specimen elongations at fracture critical point were obtained. The traditional J-integral based fracture mechanics and micromechanics based fracture models (VGM and SMCS) were applied to predict fracture in each tested local connection through refined three-dimensional FEM. Comparisons between these numerical approaches and experimental observations in prediction of fracture critical displacement, indicated that the VGM and SMCS models were able to predict fracture of welded connection with good accuracy, while the J-integral based approach resulted in quite conservative fracture prediction. This paper has bridged the gap between small-scale material tests and large-scale structural experiments in fracture evaluations.

Keywords: steel connection, micromechanics based models, fracture mechanics, J-integral, fracture prediction

1. Introduction

Improvements for the beam-to-column connections in SMRFs included use of notch-toughness rated steel and weld metal (Barsom, 2002), removal of weld backing bar and reinforcing a fillet weld, modification of weld access holes (Ricles *et al*., 2002), as well as new connection configurations such as reduced beam section (Uang *et al*., 2000; Jones *et al*., 2002) and several reinforced connection designs (Chen *et al*., 2004, 2006). These fracture mitigation measures had successfully eliminated the likelihood of brittle fractures which were observed during Northridge earthquake; however, certain improved connections were still susceptible to ductile cracking at the heat affected zone (HAZ) of the beam flange welds under unacceptable low hinge rotations (Stojadinović *et al*., 2000). The ductile fracture usually initiated from the geometric discontinuities which led to concentrations of plastic strains and triaxial stresses.

The traditional fracture mechanics parameters, such as stress intensity factor, J-integral and crack tip opening displacement are limited by the inherent assumptions of well-constrained or small-scale yielding (Kanvinde *et al*., 2004). Considerable earlier studies (e.g. Righiniotis *et al*., 2000; Righiniotis and Hobbs, 2000; Chi *et al*., 2000; Matos and Dodds, 2001, 2002; Chen *et al*., 2004a, 2004b; Wang *et al*., 2010) demonstrated that traditional fracture mechanics provided effective approaches to predict brittle fracture in pre-Northridge connections where initial flaws were often inspected at the grooved weld roots. However, it is questionable to apply traditional fracture mechanics to ductile fracture prediction at locations without macroscopic initial cracks or locations involved in large-scale yielding.

Compared to traditional fracture mechanics, recently developed micromechanics based fracture models could capture the triaxial stresses and plastic strains which directly related to ductile fracture initiation (Kanvinde *et al*., 2004; Chi *et al*., 2006). The void growth model

Note.-Discussion open until February 1, 2012. This manuscript for this paper was submitted for review and possible publication on March 18, 2011; approved on September 1, 2011.

*Corresponding author
Tel: +86-10-6278-8623; Fax: +86-10-6278-8623
E-mail: wang-yq@mail.tsinghua.edu.cn

(VGM) developed by Rice and Tracey (1969) and the stress modified critical strain (SMCS) model based on the research of Hancock and Mackenzie (1976) showed promise in predicting ductile fractures. The VGM and SMCS models for a variety of American and Japanese steels were calibrated by smooth notched tensile (SNT) tests and validated by blunt notched compact tension tests conducted by Kanvinde and Deierlein (2006). Subsequent applications to a series of twelve pull-plate tests that represented net section conditions in bolted and reduced beam section connections had shown ability of the VGM and SMCS models to predict ductile fracture initiation in steel components (Kanvinde and Deierlein, 2007). Twenty-four fillet welded cruciform tensile specimens were conducted by Kanvinde *et al*. (2008, 2009) to compare the relative accuracy of J-integral based approach and the SMCS model in predicting fracture of fillet welds, indicating that the SMCS model showed better accuracy.

This paper began with an introduction to ductile fracture mechanism and micromechanics based models. The VGM and SMCS models were calibrated for a 345 MPa grade Chinese structural steel and the corresponding weld, based on the SNT tests performed by Liao and Wang (2010). A series of seven local connections representative of the beam-to-column connections in SMRFs were tested under monotonic tensile loading. Complementary three-dimensional finite element model (FEM) analyses for all the local connection tests were then presented along with the methodologies for predicting ductile fracture using traditional J-integral based fracture mechanics and micromechanics based fracture models (VGM and SMCS). After presenting the experiments and FEM simulations, numerical based fracture predictions were compared to the experimental results. This paper aimed to bridge the gap between small-scale material tests and large-scale structural experiments in fracture predictions by using the fundamental micromechanics based fracture models.

2. Micromechanics based fracture models

2.1. Ductile fracture mechanism

Affected by temperature, stress state, loading rate and material microstructure, fracture of steel materials can generally be distinguished between ductile and brittle mechanisms. Ductile mechanisms are accompanied by large-scale plasticity and growth of microvoids, while brittle mechanisms are characterized by transgranular or intergranular cleavage. Structural steels in civil engineering applications typically exhibit ductile fracture involved with significant yielding. Schematically shown in Fig. 1, ductile fracture process contains those stages of microvoid nucleation, growth and coalescence (Anderson, 2004). Voids nucleate as a result of debonding of secondary particles or inclusions from the steel matrix when sufficient stresses are applied. After nucleation, hydrostatic stresses and plastic strains expand the voids, resulting in strain localization between the voids. Under increasing loading, material between the voids suffers local necking instabilities and the voids coalesce to form a macroscopic fracture surface.

Microvoid coalescence was frequently observed in previous round bar tensile tests at ambient temperature performed by Wu (2004). As shown in the Scanning Electron Micrograph (SEM) of Fig. 2, the central penny-shaped surface of a standard tensile specimen fabricated from Q345 structural steel was rough with dimples which

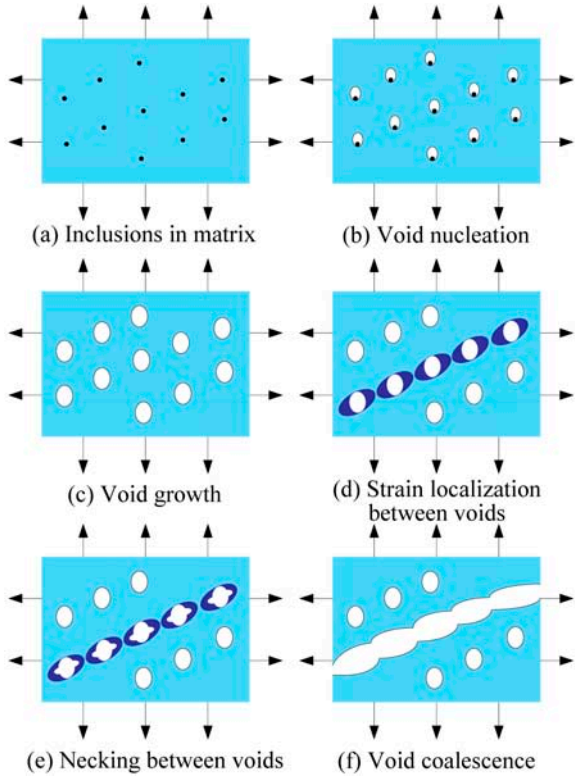

Figure 1. Mechanism of void nucleation, growth and coalescence in ductile metal (adapted from Anderson, 2004).

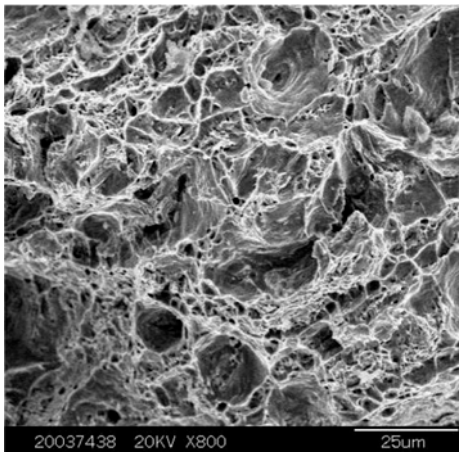

Figure 2. SEM of dimpled fracture surface of round bar tensile test specimen (Q345) (Wu, 2004).

indicated the locations of coalesced voids.

2.2. The void growth model

In most ductile metals, void growth and coalescence generally control the ductile fracture initiation. McClintock (1968) and Rice and Tracey (1969) derived analytical solutions for the growth of a single cylindrical and spherical void under plastic strains in a triaxial stress field and suggested that the void growth rate was proportional to the exponential of stress triaxiality. Based on the early work of Rice and Tracey (1969) and Hancock and Mackenzie (1976), Chi *et al*. (2006) and Kanvinde *et al*. (2006) had developed two models (i.e. VGM and SMCS) to predict ductile fracture capturing combined effects of stress triaxiality and plastic strain on the growth of microvoids. For a single spherical void, the void growth rate is given by Eq. (1) (Rice *et al*., 1969; Kanvinde *et al*., 2006):

$$dr/r = C\cdot\exp(1.5T)\cdot d\varepsilon_p \tag{1}$$

where r is the instantaneous void radius; $T=\sigma_m/\sigma_e$ is stress triaxiality (ratio of hydrostatic or mean stress σ_m to effective or von Mises stress σ_e); C is a constant; and $d\varepsilon_p=\sqrt{(2/3)d\varepsilon_{ij}^p\cdot d\varepsilon_{ij}^p}$ is the incremental equivalent plastic strain. Integrating Eq. (1), total void growth during a plastic loading excursion is expressed as:

$$\ln(r/r_0)=\int_0^{\varepsilon_p} C\cdot\exp(1.5T)\cdot d\varepsilon_p \tag{2}$$

where r_0=initial void radius. Assuming void growth to be the controlling step of fracture process, ductile fracture occurs when void growth ratio reaches a critical value described in Eq. (3):

$$\ln(r/r_0)^{critical}=\int_0^{\varepsilon_p^{critical}} C\cdot\exp(1.5T)\cdot d\varepsilon_p \tag{3}$$

The above formulation can further form the failure criterion of VGM expressed as:

$$VGM=\int_0^{\varepsilon_p}\exp(1.5T)\cdot d\varepsilon_p-\eta \tag{4}$$

where, the first term at the right hand side of Eq. (4) represents the void growth demand; η is the material capacity determined by critical void growth ratio according to Eq. (3) and described as Eq. (5):

$$\eta=\ln(r/r_0)^{critical}/\mathrm{C}=\int_0^{\varepsilon_p^{critical}}\exp(1.5T)\cdot d\varepsilon_p \tag{5}$$

For predicting fracture of a certain material point using the VGM model, refined continuum FEM analyses should be conducted to record the stress triaxiality and plastic strain history, and incrementally calculate the integration term in Eq. (4). When the void growth demand exceeds the material toughness capacity η, i.e. fracture index *VGM* in Eq. (4) exceeds zero, fracture is predicted to occur.

2.3. The stress modified critical strain model

As per Eq. (4), the VGM model explicitly integrates the triaxiality with respect to plastic strain during a loading history. However, in many realistic conditions the stress triaxiality remains largely unchanged whereas the plastic strain increases rapidly (Kanvinde *et al*., 2004). In this case, the term inside the integral of Eq. (3) can be represented as a product and reduces to the following:

$$\ln(r/r_0)^{critical}=C\cdot\exp(1.5T)\cdot\varepsilon_p^{critical} \tag{6}$$

This leads to the critical equivalent plastic strain expressed as:

$$\varepsilon_p^{critical}=\ln(r/r_0)^{critical}/[C\cdot\exp(1.5T)]=\alpha\cdot\exp(-1.5T) \tag{7}$$

where, α is a material dependent constant. The SMCS fracture criterion is simply the difference between the imposed plastic strain ε_p and the critical equivalent plastic strain given by Eq. (7). This implies that fracture will initiate when the fracture index *SMCS* exceeds zero, i.e.

$$SMCS=\varepsilon_p-\varepsilon_p^{critical}=\varepsilon_p-\alpha\cdot\exp(-1.5T) \tag{8}$$

Ductile fracture initiation is quantified as global behavior and not single material point behavior, and therefore a length scale parameter needs to be included in either the VGM or SMCS model to collect enough material failures (Kanvinde *et al*., 2004). Thus, a characteristic length l^* is introduced to complete the fracture criterion represented by Eqs. (4) and (8). The model states that ductile fracture initiation is triggered once the fracture index *VGM* or *SMCS* exceeds zero over the characteristic length l^*.

3. Calibration of VGM and SMCS models

3.1. Smooth notched tensile (SNT) tests

The material dependent parameter for each model (η in VGM or α in SMCS) can be calibrated by tests and continuum FEM analyses of SNT specimens as shown in Fig. 3. The specimen has the same geometry as standard round tensile coupon (GB/T 228, 2002) except for a circumferential notch machined into it to create a triaxial stress condition. Typically, ductile crack initiation depends on both material toughness parameter (η or α) and the characteristic length l^*. Since the contour of fracture index *VGM* or *SMCS* is very flat at the center of the notched bar (0~0.5 mm distance from center shown later in Fig. 8), ductile fracture initiation is assumed to take place simultaneously over most central portion of the critical cross-section in SNT specimen. This means fracture index *VGM* or *SMCS* is insensitive to the characteristic length in the SNT specimen, which is suitable for the calibrations of material toughness parameters η and α.

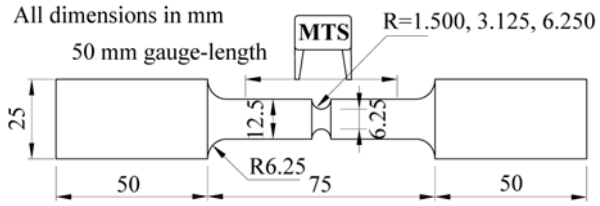

Figure 3. SNT specimen for VGM and SMCS calibration.

In order to calibrate the VGM and SMCS models for Q345 steel and the corresponding weld, eighteen SNT samples extracted from the Tee-joint weldments were tested by Liao *et al*. (2010). The Tee-joint weldment was fabricated from two 40 mm-thick steel plates and welded with complete joint penetration (CJP) by CO_2 GMAW procedure. The SNT specimens were sampled from base metal, weld metal and weld HAZ of the Tee-joint weldments, respectively. Two duplicate samples for each material with three different notch radii (i.e. R=1.5 mm, 3.125 mm and 6.25 mm) were performed. The different notch severities provided variations of stress triaxiality at the notched section where ductile fracture initiated. The SNT tests were conducted on an electronic universal testing machine and the load versus notch elongation curve for each specimen was obtained, where the elongation was measured over a 50mm gauge length as shown schematically in Fig. 3.

The load versus notch elongation curves for Q345 steel SNT specimens with three notch sizes were shown later in Fig. 6. The initial gradual loss in strength was associated with localized yielding and necking in the notch area and the sudden change in slope indicated the critical point of ductile crack initiation. Denoted by Δ_f, the elongation at fracture initiation was used as the controlling displacement in companion FEM analyses to back-calculate the material toughness parameters η and α. The cup-cone fractured surface of the SNT specimen (Liao *et al*., 2010) indicated that the ductile crack initiated in the center and propagated outward until it changed to tearing.

3.2. Finite element simulations of SNT tests

Continuum finite element simulations were conducted by ABAQUS software (ABAQUS, 2008) in analyzing the SNT test data to obtain the material toughness parameters that define the VGM and SMCS fracture criterions. The FEM analyses employed nonlinear, large deformation material models and geometrical nonlinearity of the system. The plasticity behavior was modeled by incremental theory using von Mises yield surface and isotropic strain hardening (which was suitable for steels under monotonic loading). During the standard round bar tensile test for obtaining stress-strain data, the extensometer was usually removed when the bar started to neck in an unstable mode and the strains were no longer uniform across the gauge length. However, it was necessary to recover the strains after the extensometer was removed since the strains at ductile crack initiation were much larger than those at necking. The true stress and strain at fracture was calculated according to Eqs. (9) and (10) which were derived from the conservation of volume arguments (Kanvinde *et al*., 2004).

$$\varepsilon_f=\ln[(d_0/d_f)^2] \tag{9}$$

$$\sigma_f=F_f/(\pi d_f^2/4) \tag{10}$$

where d_0 and d_f are the initial and failure diameter of the bar. The last point of the true stress versus plastic strain curve shown in Fig. 4 was obtained by such a method. The true stress versus plastic strain curve before extensometer removed was fitted by Holomon relationship as indicated in Fig. 4.

Since the calibrations of the material toughness parameters are sensitive to the stress-strain properties, a unified and representative stress-strain curve (such as the one shown in Fig. 4) is required in FEM. The true stress versus plastic strain curves for Q345 steel base metal, weld metal and weld HAZ in FEM of this study (shown in Table 1) were based on the standard round bar tensile tests performed by Liao *et al*. (2010).

Taking advantage of symmetry, two dimensional

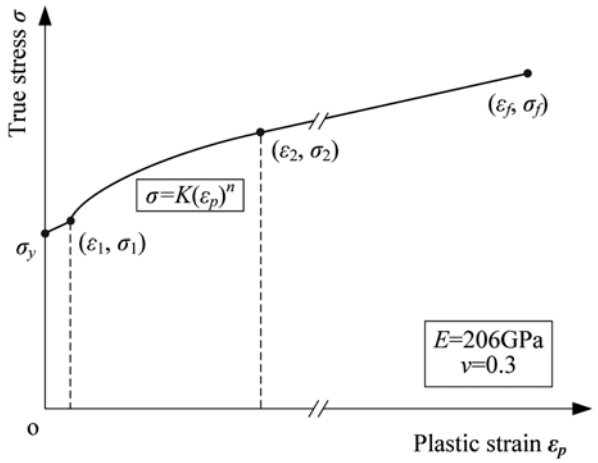

Figure 4. Schematic plot of true stress-plastic strain curve.

Table 1. Data for true stress versus plastic strain curve

Material	Base metal	Weld metal	Weld HAZ
σ_y (MPa)	323.9	391.4	361.2
ε_1	0.0067	0.0230	0.0105
σ_1 (MPa)	341.0	416.6	374.7
ε_2	0.2000	0.2000	0.2000
σ_2 (MPa)	646.6	615.8	635.3
ε_f	1.3300	1.3300	1.3000
σ_f (MPa)	1224.6	1168.4	1186.2
K (MPa)	875.6	823.6	847.5
n	0.1884	0.1807	0.1791

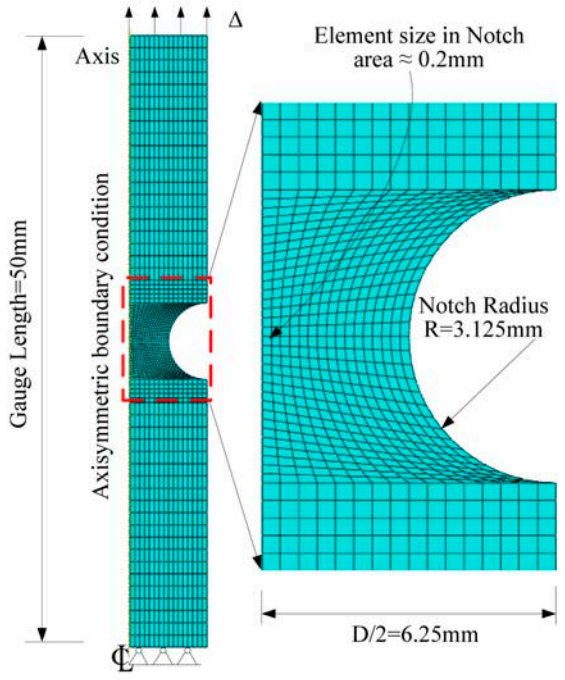

Figure 5. Axisymmetric FEM of SNT (R=3.125 mm).

axisymmetric FEMs with element type of CAX4 were modeled for the SNT specimens. As shown in Fig. 5, the element size was refined to about 0.2 mm in the notch region, which was comparable to the material characteristic length *l** mentioned afterwards in section 3.4. The FEM analyses of load versus elongation curves agreed very well with the measured test data for all the specimens with three notch sizes as shown in Fig. 6 (a), (b) and (c).

3.3. Determination of material parameters η and α

Figure 7 showed the variations of equivalent plastic strain and stress triaxiality obtained from FEM analyses at the critical displacement Δ_f when ductile fracture initiated. For specimen with notch radius R=1.5 mm or 3.125 mm shown in Fig. 7(a), the equivalent plastic strain was largest at the surface and dropped off toward the center of the bar. For specimen with R=6.25 mm, the equivalent plastic strain developped simultaneously across the whole section as a result of a larger notch radius. However, the triaxiality shown in Fig. 7(b) was largest in the center, following from the fact of highest constraint in the center. The critical equivalent plastic strain in the center of the specimen with a larger notch (R=3.125 mm) was about 42% larger than that with a smaller one (R=1.5 mm), whereas the triaxiality of the larger notched specimen (R=3.125 mm) was approximately 25% lower than that of the smaller notched specimen (R=1.5 mm). The contradiction between the point of maximum equivalent plastic strain (at the surface) and the location of ductile crack initiation (in the center) demonstrated that equivalent plastic strain alone was not an accurate fracture index.

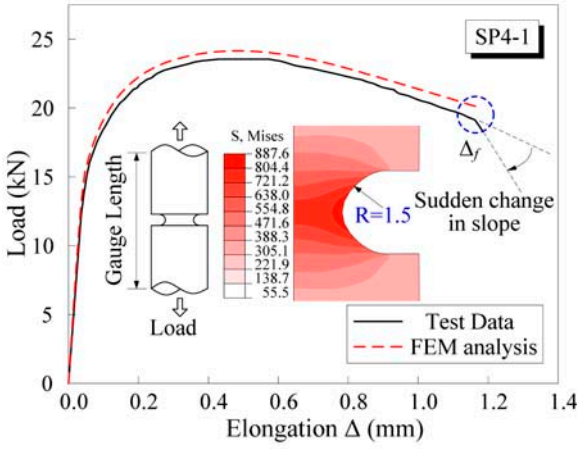

(a) SP4-1, R=1.5 mm

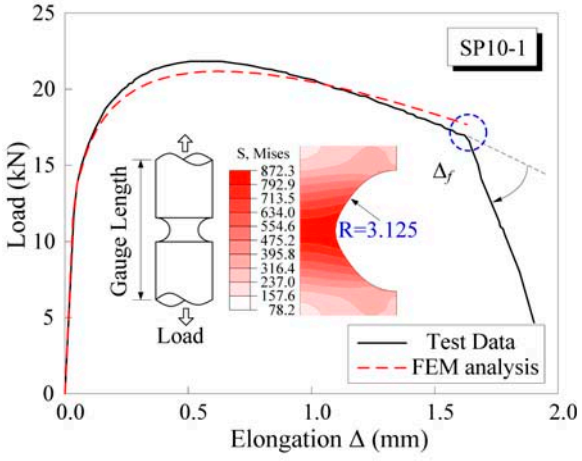

(b) SP10-1, R=3.125 mm

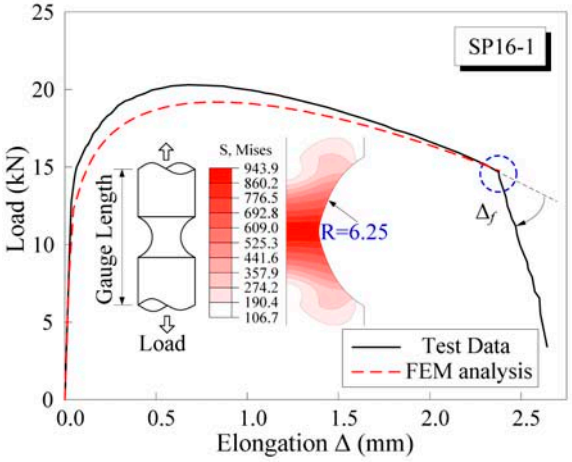

(c) SP16-1, R=6.25 mm

Figure 6. Comparison between FEM analyses and test data in load versus elongation curves for SNT specimens.

To calibrate the VGM model, FEM analyses of each SNT specimen were performed to track the stress and strain history until reaching the critical displacement Δ_f.

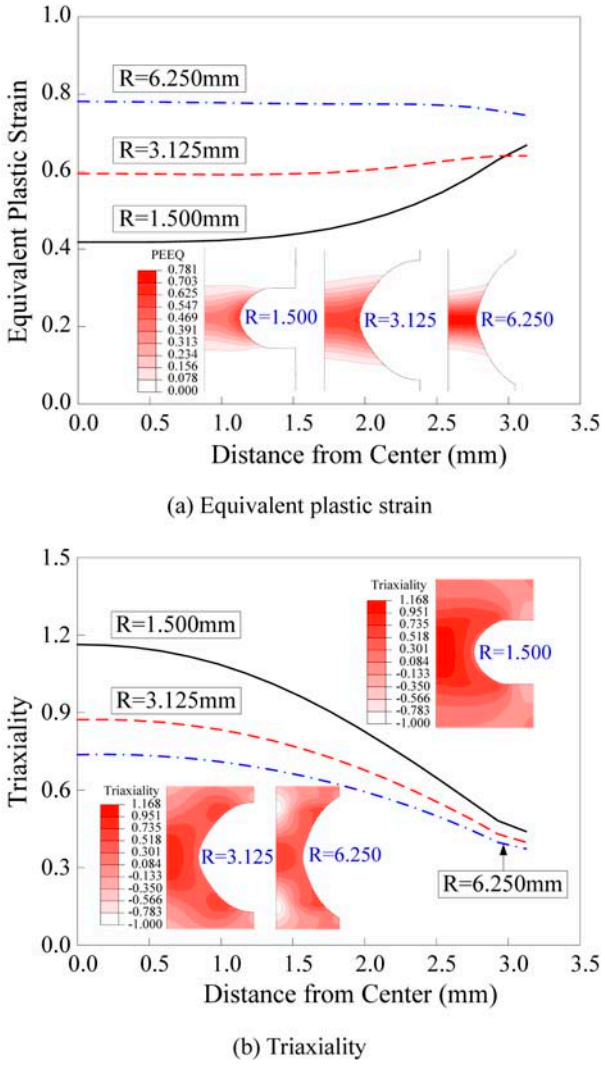

Figure 7. Variations of equivalent plastic strain and triaxiality across the notched section.

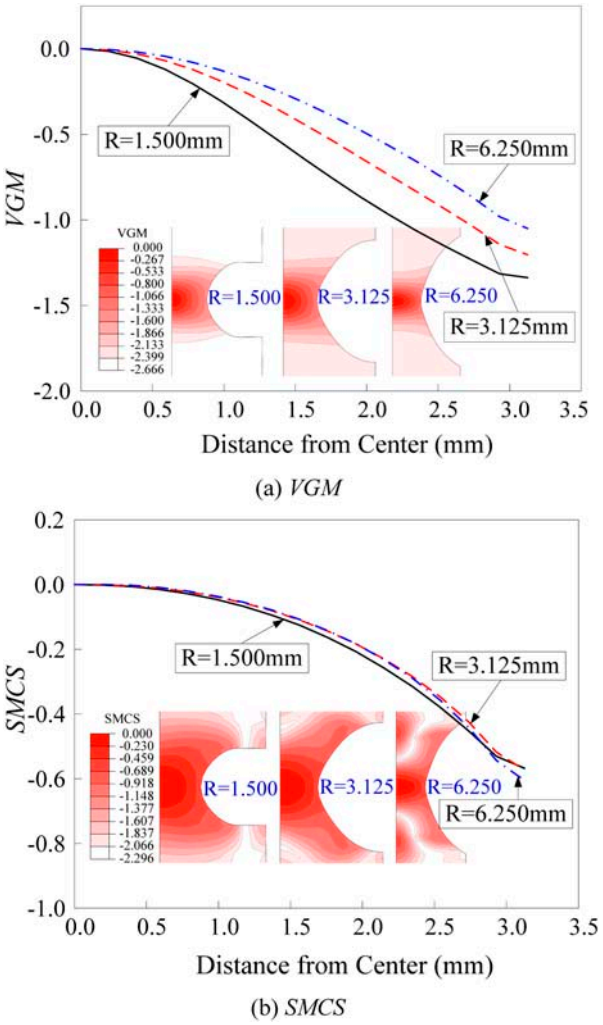

Figure 8. Variations of fracture index *VGM* and *SMCS* across the notched section.

The material toughness parameter η was determined by Eq. (5) using the stress and strain history extracted from the fracture critical point (center of the bar). The variation of fracture index *VGM* across the notched section can be obtained by substituting the material toughness parameter η and the void growth demand (integration of stress and strain history of each material point) into Eq. (4). As shown in Fig. 8 (a), consistent variation of fracture index *VGM* for the three notch sizes demonstrated the effectiveness of the VGM model in various stress states.

The calibration process for the SMCS model was similar to that for the VGM model, except for some small modifications in the expressions. FEM analysis for each SNT specimen was used to obtain the stresses and strains corresponding to the critical displacement Δ_f. The instantaneous stress and strain states from the center of the notched bar at the critical displacement were substituted into Eq. (7) to back-calculate the material toughness parameter α. As shown in Fig. 8(b), the distribution of fracture index *SMCS* was obtained by substituting equivalent plastic strain and triaxiality distributions at the critical displacement Δ_f, as well as the back-calculated d into Eq. (8). The SMCS distributions for three notch sizes were quite similar, confirming α to be a fundamental material toughness parameter that was independent of stress states.

The process of combining test and analysis results to calibrate the material toughness parameters η and α was repeated for each specimen and the results were summarized in Table 2. The fracture elongation Δ_f used as the critical displacement in FEM were directly obtained from tests performed by Liao *et al.* (2010) and the material toughness parameters η and α were calibrated in this study. The mean values and coefficients of variations (COV=standard deviation/mean value) for η and α were also reported in Table 2. The low COV of η and α (ranging from 5.2 to 15.1%) demonstrated the effectiveness of the VGM and SMCS models to simulate ductile crack initiation under varied stress conditions. Comparing the

Table 2. Summary of SNT tests for calibration of parameters η and α in VGM and SMCS models

Material	Radius (mm)	Test No.	Δ_f (mm)	η	α
Base metal	1.500	4-1	1.169	2.666	2.391
		5-1	1.260	2.931	2.555
	3.125	10-1	1.629	2.346	2.204
		11-1	1.670	2.412	2.260
	6.250	16-1	2.382	2.311	2.361
		17-1	2.405	2.339	2.391
		Mean		2.501	2.360
		COV		9.9%	5.2%
Weld metal	1.500	4-2	1.211	3.281	2.722
		5-2	1.051	2.825	2.440
	3.125	10-2	1.592	2.444	2.247
		11-2	1.505	2.302	2.128
	6.250	16-2	2.596	2.695	2.747
		17-2	2.213	2.210	2.225
		Mean		2.626	2.422
		COV		15.1%	11.0%
Weld HAZ	1.500	4-3	1.169	2.926	2.534
		5-3	1.126	2.800	2.456
	3.125	10-3	1.550	2.310	2.156
		11-3	1.585	2.367	2.204
	6.250	16-3	2.487	2.509	2.561
		17-3	2.299	2.273	2.307
		Mean		2.531	2.370
		COV		10.8%	7.3%

Table 3. Representative values of characteristic length

Material	Characteristic length l^* (mm)		
	Lower	Mean	Upper
Base metal	0.087	0.201	0.473
Weld metal	0.062	0.202	0.311
Weld HAZ	0.072	0.329	0.671

three material types, the mean values were quite similar but the COV for weld metal was a little larger.

3.4. Characteristic length

In addition to complete the VGM and SMCS model calibrations, one must consider the critical volume of material over which these fracture criteria are satisfied to form a macrocrack. This volume is represented by a characteristic length l^*, which is determined through fractographic studies based on microstructural measurements such as grain size and dimple diameter. The approach to determine the characteristic length in this study was borrowed from Hancock & Mackenzie (1976). A lower bound of characteristic length was evaluated as twice the dimple diameter of the primary voids, which corresponded to two adjacent voids coalescing. The mean or upper bound value was determined by averaging or maximizing a number of measured plateau and valley sizes observed from the SEM. Fracture surfaces of nine SNT specimens with three material types were obtained through SEM tests by Liao *et al*. (2010) and three representative values of characteristic length were listed in Table 3. The mean values of characteristic length shown in Table 3 were used in afore- and after-mentioned FEM analyses.

4. Local beam-to-column connection tests

4.1. Specimens and test setup

Shop welded steel connection is believed to have better quality than field welded connection and now it is widely applied in China. As shown in Fig. 9, the beam-to-column connection in SMRF is fabricated by welding a stub beam to the column with complete joint penetration (CJP) groove weld in the shop. Then, a long beam is linked to the stub beam with high strength bolts and CJP

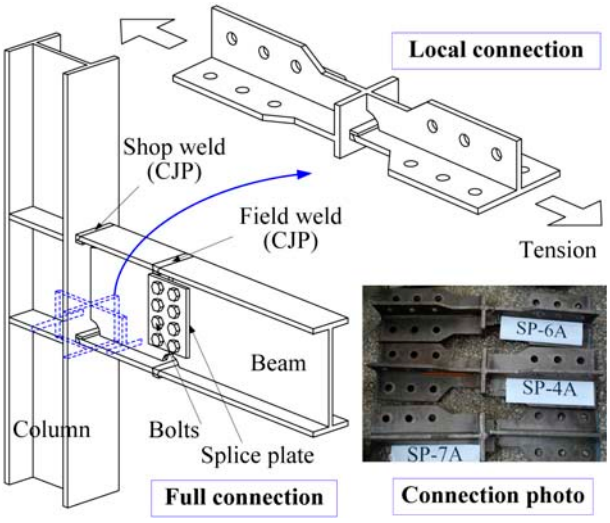

Figure 9. Full connection and local connection.

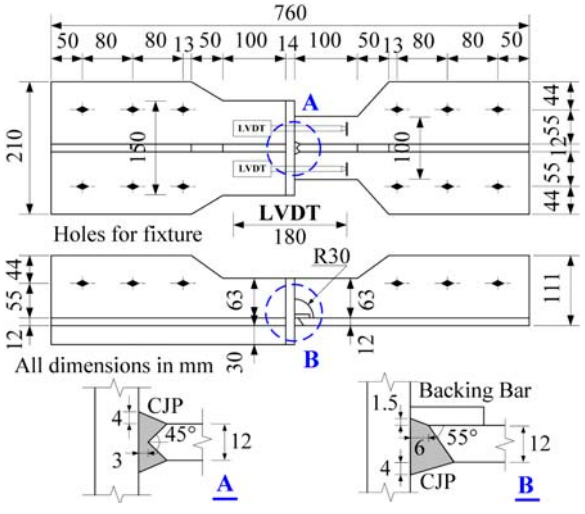

Figure 10. Geometries and weld details of local connection.

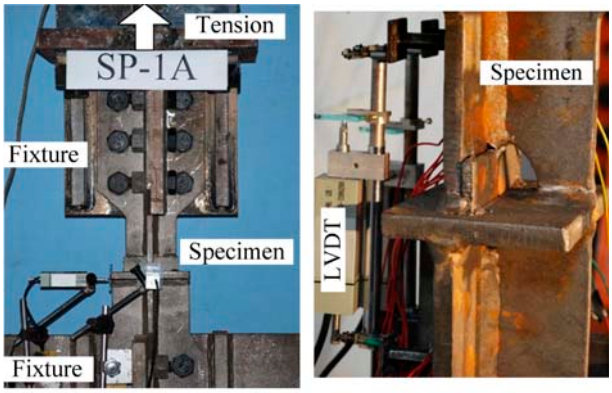

Figure 11. Photos of test setup and LVDT installation.

weld in the field. Learned from the Northridge earthquake and Kobe earthquake, it is clear that beam-to-column connections are susceptible to fracture at the bottom beam flange to column flange welds. To investigate the fracture performance of the shop welded connection, local connections (shown in Figs. 9 and 10) representing the bottom part of the full beam-to-column connection were tested under monotonic tensile loading in this study.

Geometries of the seven local connections were similar except for the width (W=80~120 mm) and thickness (t=10 or 12 mm) of the beam flange. Figure 10 showed the dimensions and weld details of specimen SP-1A. The local connections fabricated from Q345 steel plates were shop welded through GMAW (CO_2) welding procedure. The beam web was CJP welded to the column flange by double grooves (shown in Fig. 10 detail A) and the beam flange was welded by single groove with backing bar left in place (shown in Fig. 10 detail B). As shown in Figs.10 and 11, the holes at the end of the specimen were for attachment to the loading fixture with high strength bolts. Monotonic tensile loading was applied in a displacement-controlled 2000 kN capacity servo-hydraulic testing machine. Two displacement transducers LVDT (Linear Variable Differential Transformer) shown in Fig. 11(b) were attached to either side of the specimen to monitor the elongation over the central 180mm gauge length, where the average displacement measurements were used for comparison with the FEM analyses.

4.2. Test results

With average data from the two displacement transducers LVDT, load versus elongation curves of the tested local connections were obtained (shown later in Fig. 22). The ultimate load capacity P_u, the critical elongation Δ_f and the corresponding load capacity P_f indicated by the load versus elongation curves were listed respectively in Table 4.

As shown in Table 4, specimens with larger flange width W (SP-4A, SP-8A & SP-9A) seemed to fracture earlier with smaller elongations, while specimens with

Table 4. Test results of the local connections.

Specimen No.	W (mm)	t (mm)	P_u (kN)	P_f (kN)	Δ_f (mm)
SP-1A	100	12	883.5	882.3	7.85
SP-4A	100	12	849.9	844.4	4.29
SP-5A	100	10	815.4	774.2	6.14
SP-6A	80	12	772.4	745.4	7.80
SP-7A	90	12	831.3	828.8	5.30
SP-8A	110	12	880.1	830.9	3.05
SP-9A	120	12	976.5	976.1	3.24

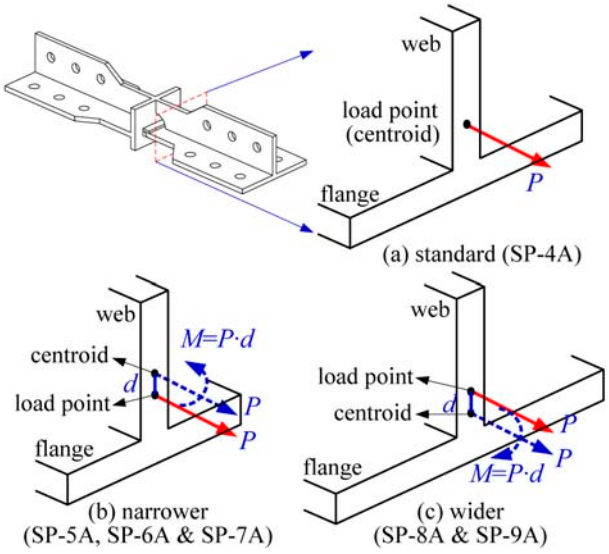

Figure 12. Schematic plot of eccentric load on the section.

smaller flange width W (SP-5A, SP-6A & SP-7A) fractured with larger elongations. This was mainly because of the load eccentricity which introduced an additional moment on across-section of the location connection. Shown in Fig. 12(a), the load point was designed to superpose on the section centroid of specimen SP-4A so as to produce uniform stresses on the section. The load points were kept in the same location as specimen SP-4A whereas the flange width varied for other specimens. As shown in Fig. 12(b), centroid of specimen with narrower flange raised up from the load point, and therefore more stresses were imposed on the beam flange. While in Fig. 12(c), centroid of specimen with wider flange dropped down and more stresses were added to the beam web.

As it was reduced by the weld access hole, the beam web section was more critical to fracture failure under uniform nominal stresses. When the eccentric load imposed more stresses on the beam web of specimen with wider flange, it accelerated fracture initiation in the beam web. As for specimen with narrower flange, less loading was sustained by the beam web and therefore larger elongation at fracture was achieved. As shown in Fig. 13, cracks in local connection SP-4A, SP-8A and SP-9A

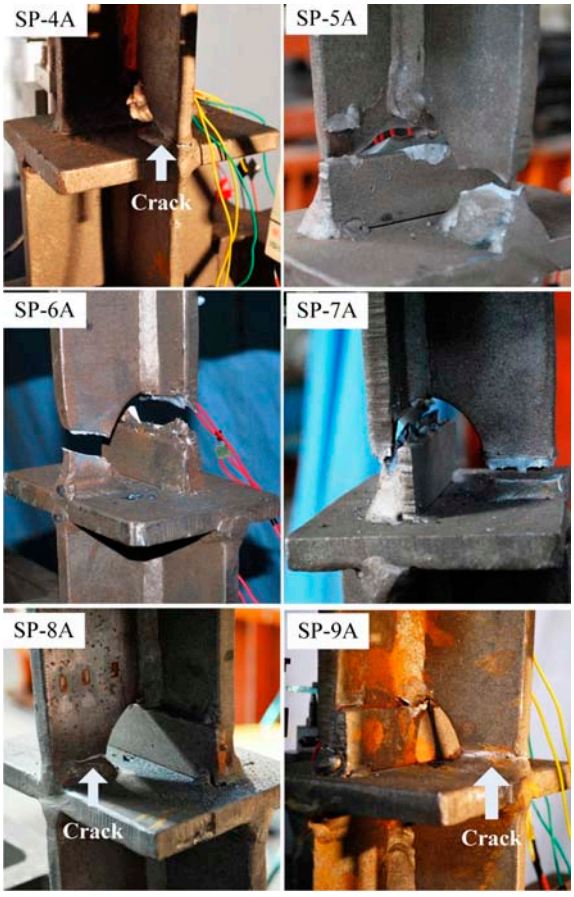

Figure 13. Fracture modes of the local connections.

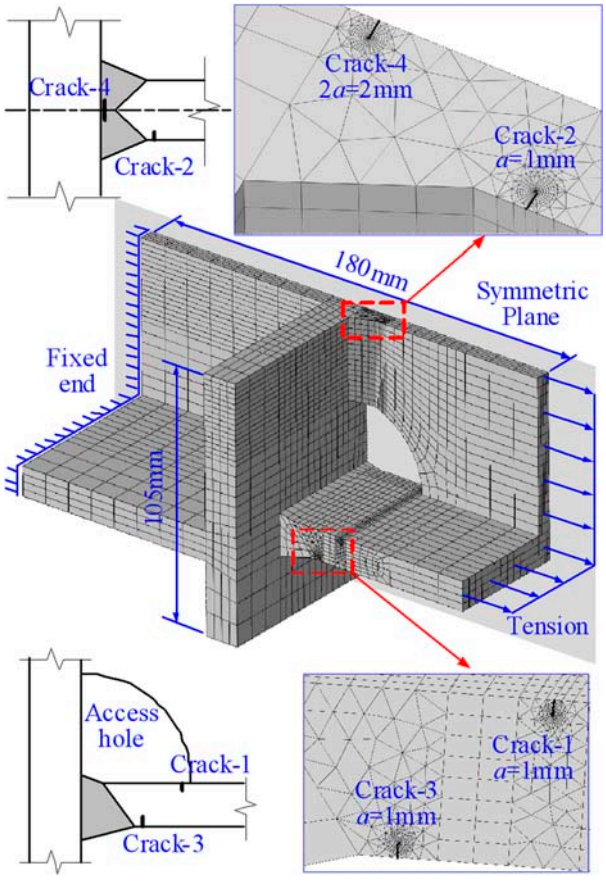

Figure 14. FEM of local connection with assumed cracks.

(with wider flanges) initiated from beam web welds or HAZ, while fractures in connection SP-5A, SP-6A and SP-7A (with narrower flanges) initiated from beam flange at the toe of weld access hole and propagated across the whole section.

5. FEM simulations of the local connections

5.1. Fracture prediction using fracture mechanics

The segment with 180mm gauge length of the local connection was modeled using ABAQUS/CAE (2008) according to the geometries shown in Fig. 10. Taking advantage of symmetry, half model (shown in Fig. 14) was employed in the FEM simulations. The three dimensional FEM contained approximately 25,000 hexahedral elements (C3D8). The model was fixed at one end and loaded by displacement control at the other end. The stress and strain properties of Q345 steel base metal and weld metal were explicitly modeled in FEM with large deformation theory and isotropic incremental von Mises plasticity. The material model of base metal was calibrated by stress-strain data from uniaxial tensile tests (GB/T 228, 2002) of Q345 steel used in the local connection specimens. The key points of stress-strain curve as shown in Fig. 4 were almost the same as base metal listed in Table 1, except σ_y=369.1 MPa, σ_1=419.0 MPa and ε_1=0.02. The material model of weld metal used the stress-strain data listed in Table 1, since the weld metal in the specimens had not been tested.

As shown in Fig. 14, four cracks were simulated to investigate the fracture behavior of the critical parts, i.e. beam flange near the toe of weld access hole (Crack-1), the weld toes (Crack-2 and Crack-3) and the fusion line of beam web weld to column flange (Crack-4). Crack-1 to Crack-3 were assumed to be the Mode I exterior through crack with depth a=1 mm, while Crack-4 was an interior crack with half depth of 1mm to simulate unfused part of the weld. Refined mesh (seven contours around the crack tip and twenty-four elements for each contour) was achieved by mesh convergence study based on the accuracy of J-integral calculation. The J-integral (J_I) calculated by FEM was applied as a fracture mechanics parameter to quantify the fracture toughness demand near a crack tip. The corresponding material fracture toughness J_{IC} could be determined by standard fracture tests, such as three point bending or compact tension test (GB/T 21143, 2007). Thus, fracture was predicted to occur when fracture toughness demand J_I exceeded the material fracture toughness capacity J_{IC}, i.e. when $J_I > J_{IC}$.

Figure 15 showed the variations of fracture toughness demand J_I through cracks under yield loading F=721.5

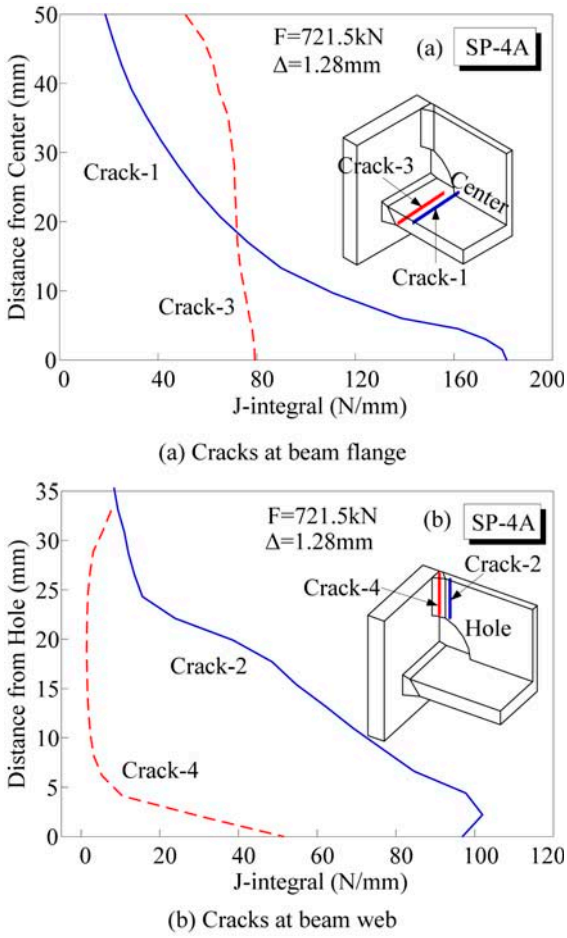

Figure 15. Distributions of J-integral at Δ=1.28 mm

kN (Δ=1.28 mm). Indicated by Fig. 15(a), J-integral decreased from center of the beam flange both for Crack-1 and Crack-3, but more fracture toughness was required by Crack-1. As shown in Fig. 15(b), J-integral for Crack-2 was much larger than that for Crack-4 and it was largest near the edge of weld access hole. These results helped to explain the large likelihood of fractures at locations of Crack-1 and Crack-2 in the tested local connections (shown in Fig. 13).

Further analyses were performed for Crack-1 and Crack-2 by applying incremental elongation up to 8 mm at the end of the model. Figure 16 showed the fracture toughness demand J_I (at the largest location of Crack-1 or Crack-2) versus elongation curves for local connection SP-4A to SP-9A and J_I increased with the increment of elongation. As shown in Fig. 16, the critical elongation at which point fracture occurred was predicted by the demand curve and the corresponding material toughness capacity. Here, fracture toughness J_{IC}=372.4 N/mm for Q345 base metal was the average value of test data obtained by Wu (2004) and Wu *et al.* (2004) and J_{IC}=235.8 N/mm for weld HAZ was based on the test results of Liu *et al.* (2002). Since Crack-1 and Crack-2 were located in base metal and weld HAZ, respectively, different material fracture toughness were selected. The critical elongations for connection SP-4A, SP-5A, SP-8A and SP-9A were determined by curves of Crack-1, while for SP-4A and SP-7A critical elongations were controlled by Crack-2.

5.2. Fracture prediction using VGM and SMCS

Compared to sharp cracks, blunt notches seemed to be

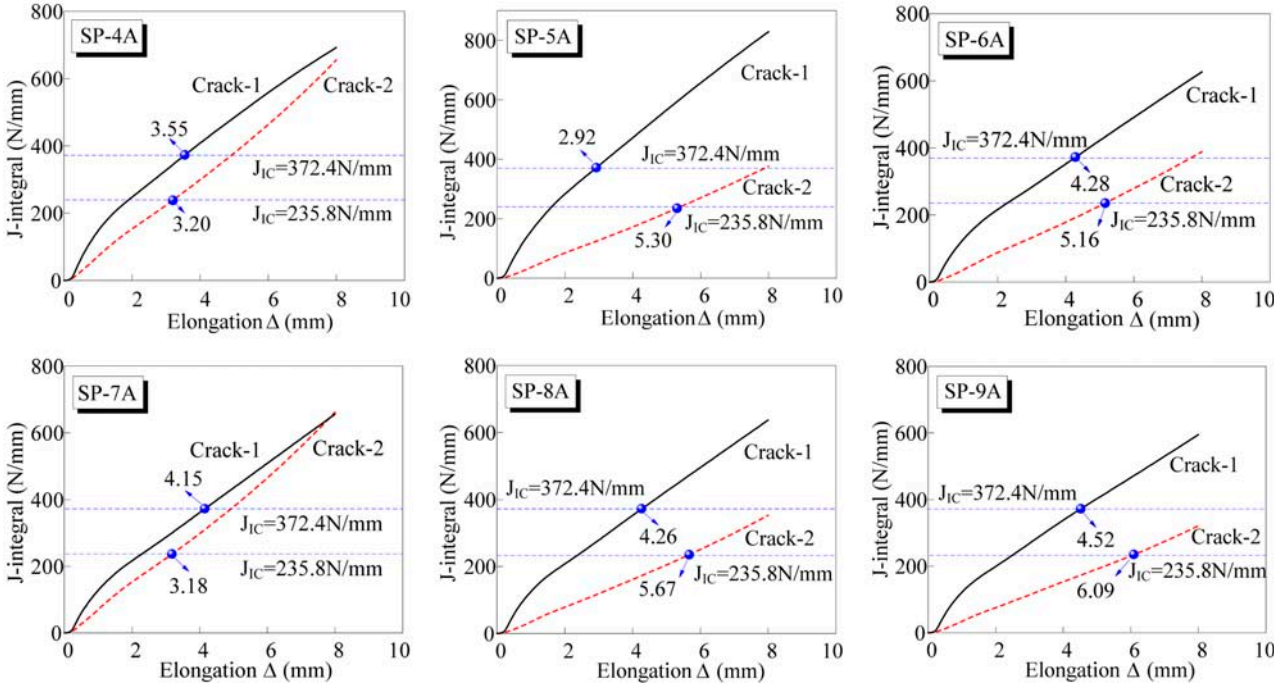

Figure 16. J-integral versus elongation curves for local connection SP-4A to SP-9A.

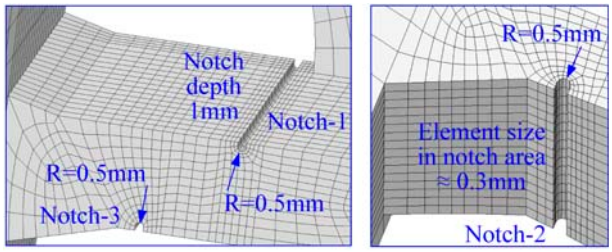

(a) Beam flange notches (b) Beam web notch

Figure 17. Meshes around the notches in VGM and SMCS finite element models.

more realistic in simulating weld and geometry defects in the local connections. As shown in Fig. 17, three notches replacing cracks at fracture critical parts were introduced in the FEM. All the three blunt notches were 1mm in depth and 0.5 mm in radius. Material properties and boundary conditions were the same as the above mentioned fracture mechanics models. The FEM contained nearly 17,000 hexahedral elements (C3D8), where the smallest elements around the notches were in the order of 0.3 mm. This element size was comparable to the characteristic length l^* as listed in Table 3.

In order to predict ductile fracture initiation using the VGM and SMCS criteria, the stress and strain data of the local connection FEM were monitored during the loading history of increasing displacement up to 8mm. ABAQUS provides user-defined subroutines to define output variables that are functions of any available parameters calculated at integration points. A FORTRAN subroutine given in Appendix was applied to calculate fracture indices *VGM* and *SMCS* as per Eqs. (4) and (8). The average values of calibrated material toughness parameters η=2.501 and α=2.360 (summarized previously in Table 2) were used for calculation of Eqs. (4) and (8). The user-defined subroutine got calculated values of von Mises stress, mean stress and equivalent plastic strain at integration points and output five user-defined variables (including *VGM* and *SMCS*) within each increment. The contours of user-defined output variables (such as fracture indices *VGM* and *SMCS*) at the integration points could be plotted with visualization module in ABAQUS/CAE (2008).

Variations of fracture indices *VGM* and *SMCS* along the notches were shown in Figs. 18 and 19, respectively. Line plots of *VGM* and *SMCS* distributions on the two loading levels (Δ=1.36 mm and 4.80 mm) indicated that *VGM* and *SMCS* values increased with the increment of elongations. For Notch-1 across the width of beam flange, *VGM* and *SMCS* were largest in the central part just near the toe of weld access hole. For Notch-2 along the toe of beam web to column flange weld, *VGM* and *SMCS* were largest at the location where it was about 3 mm distance away from the edge of weld access hole. Fracture indices *VGM* and *SMCS* values for Notch-3 were relatively lower than those for Notch-1 and Notch-2, indicating that the local connections would probably not fracture at the toe

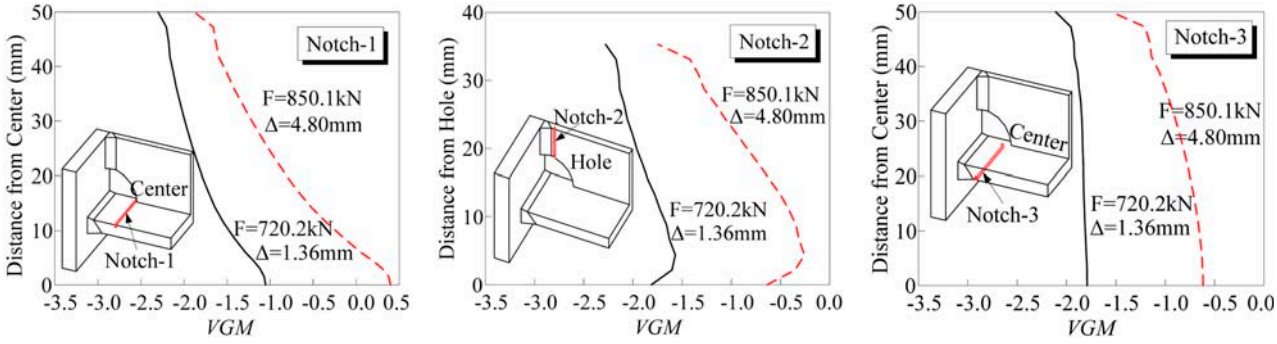

Figure 18. Distributions of fracture index *VGM* along the notches at elongation Δ=1.36 mm and 4.80 mm.

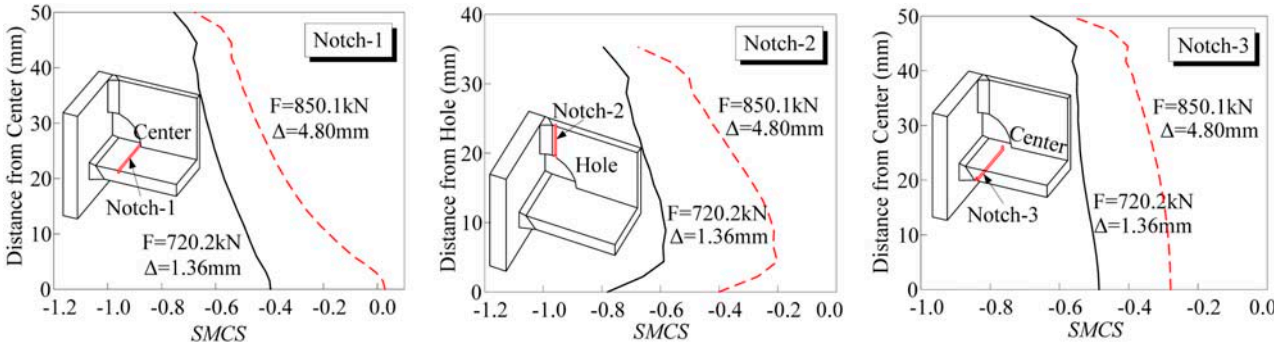

Figure 19. Distributions of fracture index *SMCS* along the notches at elongation Δ=1.36 mm and 4.80 mm.

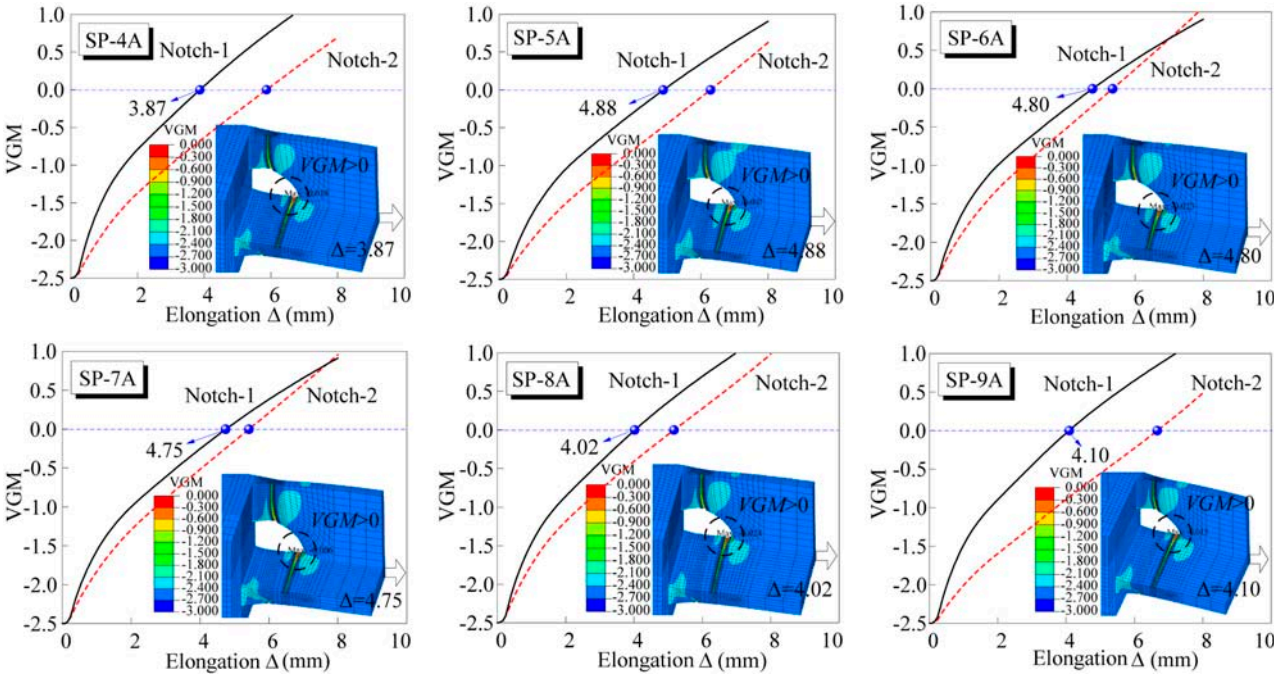

Figure 20. *VGM* versus elongation curves and *VGM* contour plots for local connection SP-4A to SP-9A.

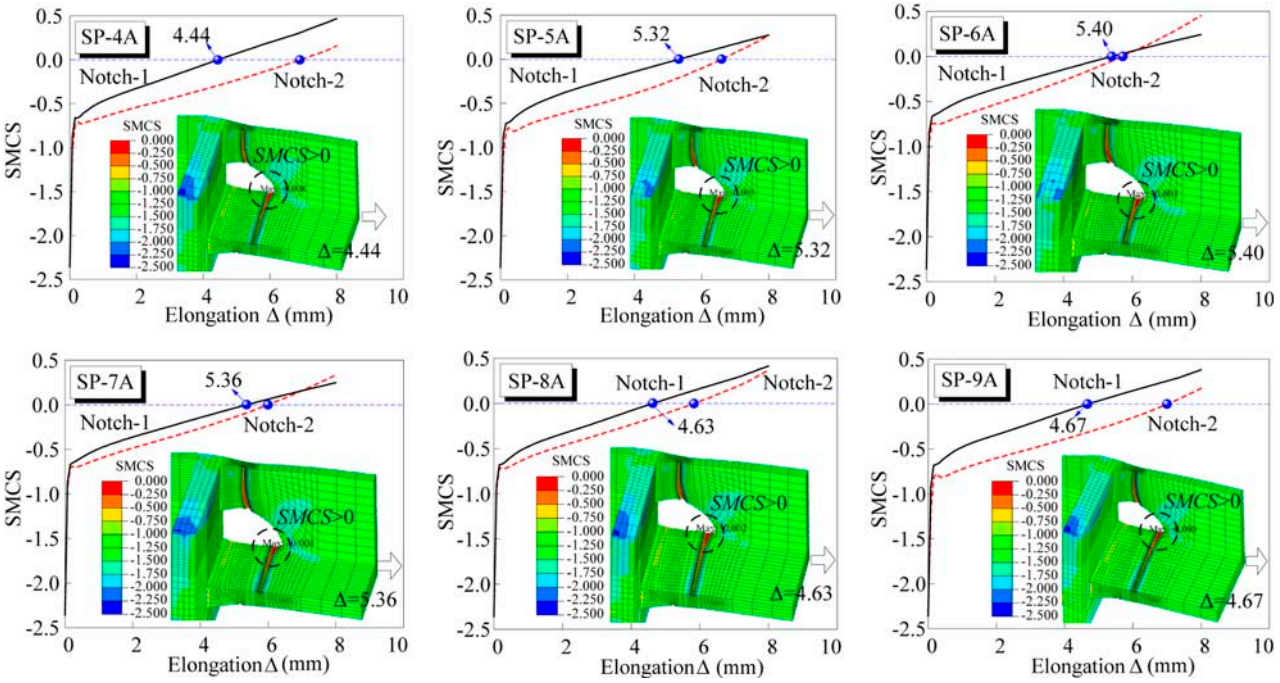

Figure 21. *SMCS* versus elongation curves and *SMCS* contour plots for local connection SP-4A to SP-9A.

of beam flange to column flange weld.

The locations with the largest *VGM* or *SMCS* value along Notch-1 and Notch-2 were monitored during the entire loading history. The *VGM* or *SMCS* versus applied elongation curves for local connection SP-4A to SP-9A were shown in Fig. 20 and Fig. 21, respectively. The *VGM* or *SMCS* contour plots obtained through user-defined output subroutine showed the largest value in the center of the beam flange, indicating the fracture initiation point. With the line plots of *VGM* or *SMCS* versus elongation curves, ductile fracture initiation was predicted when fracture index *VGM* or *SMCS* exceeded zero and the corresponding critical elongation was pointed out in Fig. 20 and Fig. 21 for each specimen.

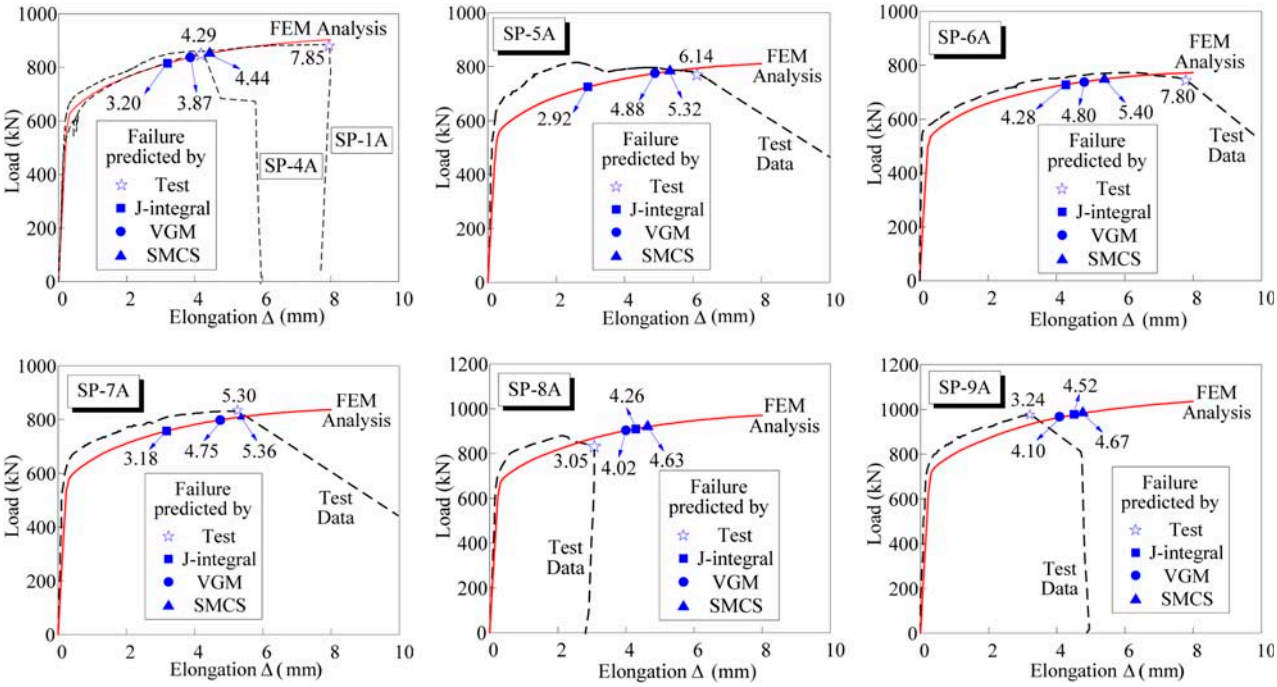

Figure 22. Comparison of FEM analyses and test results for fracture predictions in local connections.

5.3. Comparison of FEM analyses and test results

Figure 22 showed the load versus elongation curves obtained by the FEM simulations of local connections, which were overlaid on the measured test results. The load versus elongation curves predicted by the FEM analyses tracked the test results very well except for specimen SP-5A, where connection bolts for testing fixture slid in the loading history. The fracture critical elongations measured in the tests were indicated by pentacle markers on the dashed lines. The fracture critical elongations predicted by traditional J-integral based fracture mechanics and micromechanics based fracture models (VGM and SMCS) were also pointed out in Fig. 22 with different markers. Large differences in fracture critical elongations were observed in the tests of specimen SP-1A and SP-4A, whereas they were identical in geometry. This might be attributed to the large variations in material fracture toughness and initial flaw size in the weld. The test results of local connection SP-1A would be ignored in later comparisons.

For specimen SP-4A~SP-7A (with narrower beam flange), fracture predictions based on FEM analyses were conservative compared to the test results. Further comparisons about the relative accuracy of each FEM analysis approach were summarized in Table 5. Compared to the micromechanics based fracture models, traditional fracture mechanics provided a more conservative approach to predict the fracture critical elongation and sometimes it seemed to be inaccurate (error up to 110% as for specimen SP-5A). The micromechanics based fracture models were found to be effective tools to predict fracture critical elongation with good accuracy. Furthermore, the SMCS model seems to be more accurate than the VGM model in predicting fracture. Discrepancies between predicted and tested fracture critical elongations for SP-4A to SP-7A were within –3%~44% by the SMCS model and 11%~63% by the VGM model.

Table 5. Summary of test and FEM analyses results for local connections in fracture predictions

Specimen	Δ_f^{test} (mm)	$\Delta_f^{test}/\Delta_f^{analysis}$ based on			P_f^{test} (kN)	$P_f^{test}/P_f^{analysis}$ based on		
		J-integral	VGM	SMCS		J-integral	VGM	SMCS
SP-1A	7.85	2.45	2.03	1.77	882.3	1.05	1.07	1.05
SP-4A	4.29	1.34	1.11	0.97	844.4	1.01	1.02	1.00
SP-5A	6.14	2.10	1.26	1.15	774.2	1.04	1.01	1.00
SP-6A	7.80	1.82	1.63	1.44	745.4	1.00	1.02	1.01
SP-7A	5.30	1.67	1.12	0.99	828.8	1.06	1.05	1.04
SP-8A	3.05	0.72	0.76	0.66	830.9	0.89	0.92	0.92
SP-9A	3.24	0.72	0.79	0.69	976.1	0.98	1.01	1.01

For specimen SP-8A and SP-9A (with wider beam flange), both the traditional fracture mechanics and micromechanics based models tended to overestimate the fracture critical elongations. This might result from the discrepancy in loading conditions between tests and FEM simulations. On the one hand, the eccentric load in the tests of specimen SP-8A and SP-9A imposed more stresses on the weaker beam web, resulting in premature cracks in the beam web to column flange welds. On the other hand, the consistent displacement control at the end of specimen SP-8A and SP-9A in FEM simulation resulted in more stresses flowing to the stiffer beam flange. Therefore, the fracture critical elongations were overestimated by FEM predictions.

Referring again to Table 5, the load capacities at fracture critical point predicted by FEM analyses agreed very well with those obtained from the tests, but a little overestimate for specimen SP-8A and SP-9A. The reasons were the same as those for overestimations in the fracture critical elongations by FEM analyses.

6. Summary and conclusions

Micromechanics based fracture models had been developed to predict ductile fracture in steel structures by relating micro-mechanism of void nucleation, growth and coalescence to macroscopic stresses and strains. Two such models - the VGM and the SMCS models for three material types (Q345 steel base metal, weld metal and weld HAZ) were calibrated through SNT tests (Liao *et al*., 2010) and complementary FEM analyses. A series of seven local connections representing beam-to-column connections in SMRFs were tested to investigate the fracture behavior and ductility for this type of connection. Then traditional J-integral based fracture mechanics approach and micromechanics based fracture models (VGM and SMCS) were provided to predict fracture in the local connections through refined three-dimensional FEM. Fracture predictions based on the FEM analyses were compared to the test results. The following conclusions can be drawn from this study:

(1) The low COV of material toughness parameters η in VGM (ranging from 9.9% to 15.1%) and α in SMCS (ranging from 5.2% to 11.0%) demonstrated the effectiveness of VGM and SMCS models to predict ductile fracture initiation in Q345 steel base metal and weld metal. Many structural details in steel structures were without sharp cracks or flaws and involve flat stress and strain gradients, which obviate the necessity of characteristic length calibrations in VGM and SMCS models.

(2) A series of seven local connections fabricated from Q345 steel were tested under monotonic tensile loading. Three specimens fractured at the toe of beam web to column flange weld and another three fractured across the whole section, while specimen SP-1A was not loaded to fracture due to the limitation of testing machine in displacement capacity.

(3) Traditional J-integral based fracture mechanics was applied in the local connections with assumed initial cracks. Comparison of critical elongations predicted by J-integral criterion (i.e. $J_I > J_{IC}$) and measured in tests indicated that traditional fracture mechanics was too conservative to predict ductile fracture initiation in the local connections.

(4) The VGM and SMCS models were provided in ductile fracture predictions in the local connections with assumed blunt notches which were idealizations for connection initial defects. These models were able to predict the fracture critical elongations for specimen SP-4A~SP-7A with good accuracy and SMCS model was more accurate compared to VGM model.

(5) The micromechanics based fracture models showed much greater promise in predicting ductile fracture, especially for the locations without sharp cracks or subjected to large-scale yielding, where traditional fracture mechanics was invalidated.

Acknowledgment

This study is financially supported by National Natural Science Foundation of China (Grant No. 50778102 and No. 90815004).

Notation

The following symbols are used in this paper:

a= crack depth in local connection;
d_0= initial diameter of standard tensile bar;
d_f= fractured diameter of standard tensile bar;
J_{IC}= mode I material fracture toughness;
K= strength coefficient in Holomon relationship;
l^*= characteristic length;
n= strain hardening exponent;
P_f^{test}= fracture load measured in tests;
$P_f^{analysis}$= fracture load predicted by analysis;
R= notch radius in SNT specimen;
r, r_0=i nstantaneous and initial microvoid radius;
$SMCS$= fracture index for SMCS model;
T= stress triaxiality (σ_m/σ_e);
t= thickness of beam flange in local connection;
VGM= fracture index for VGM model;
W= width of beam flange in local connection;
α= material toughness parameter for SMCS;
Δ_f= fracture elongation in SNT tests or local connection tests;
Δ_f^{test}= fracture elongation measured in tests;
$\Delta_f^{analysis}$= fracture elongation predicted by analysis;
ε_p= equivalent plastic strain;
$\varepsilon_p^{critical}$= critical equivalent plastic strain;
η= material toughness parameter for VGM;
σ_e= effective or von Mises stress;
σ_m= mean or hydrostatic stress.

Appendix

```
      ************************************
      *Subroutine for VGM and SMCS calculation
      *Definition of variables
      *UVAR(1)=Triaxiality
      *UVAR(2)=Equivalent Plastic Strain (PEEQ)
      *UVAR(3)=Fracture Index SMCS
      *UVAR(4)=Fracture Index VGM
      *UVAR(5)=VGM Fracture Demand
      *VALNEW(1)=Triaxiality, instantaneous
      *VALNEW(2)=PEEQ, instantaneous
      ************************************
      SUBROUTINE UVARM(UVAR,DIRECT,T,
     +TIME,DTIME,CMNAME,ORNAME,
     +NUVARM,NOEL,NPT,NLAYER,NSPT,
     +KSTEP,KINC,NDI,NSHR,COORD,
     +JMAC,JMATYP,MATLAYO,LACCFLA)
      IMPLICIT REAL*8(a-h, o-z)
      PARAMETER (nprecd=2)
      CHARACTER*80 CMNAME,ORNAME
      CHARACTER*3 FLGRAY(15)
      DIMENSION UVAR(NUVARM),T(3,3),
     +DIRECT(3,3),TIME(2),COORD(*),
     +JMAC(*),JMATYP(*)
      DIMENSION ARRAY(15),JARRAY(15),
     +VALNEW(15)
      PARAMETER (E=2.71828,TOL=0.00001,
     +ALPHA=2.360,ETA=2.501)
      ************************************
      *Get stress values and calculate triaxiality
      ************************************
      CALL GETVRM('SINV',ARRAY,JARRAY,
     +FLGRAY,JRCD,JMAC,JMATYP,
     +MATLAYO,LACCFLA)
      IF(ARRAY(1).LE.TOL)THEN
       VALNEW(1)=0
      ELSE
       VALNEW(1)=-ARRAY(3)/ARRAY(1)
      END IF
      ************************************
      *Get PEEQ and calculate VGM & SMCS
      ************************************
      CALL GETVRM('PE',ARRAY,JARRAY,
     +FLGRAY,JRCD,JMAC,JMATYP,
     +MATLAYO,LACCFLA)
      VALNEW(2)=ARRAY(7)
      UVAR(5)=UVAR(5)+(VALNEW(2)-
UVAR(2))*E**(ABS(1.5*VALNEW(1)))
      UVAR(4)=UVAR(5)-ETA
      UVAR(1)=VALNEW(1)
      UVAR(2)=VALNEW(2)
      UVAR(3)=UVAR(2)-ALPHA*E**(-
ABS(1.5*UVAR(1)))

      RETURN
      END
```

References

ABAQUS (2008). *ABAQUS User's Manual*, *Version 6.8*. Hibbitt, Karlsson and Sorenson, Inc., Providence, RI.

Anderson, T. L. (2004). *Fracture mechanics: Fundamentals and applications, 3rd Ed.*. CRC Press, Boca Raton, Fla.

Barsom, J. M. (2002). "Development of fracture toughness requirements for weld metals in seismic applications." *Journal of Materials in Civil Engineering*, 14(1), pp. 44-49.

Chen, C. C., Lin, C. C., and Tsai, C. L. (2004). "Evaluation of reinforced connections between steel beams and box columns." *Engineering Structures*, 26(13), pp. 1889-1904.

Chen, C. C., Lin, C. C., and Lin, C. H. (2006). "Ductile moment connections used in steel column-tree moment-resisting frames." *Journal of Constructional Steel Research*, 62(8), pp. 793-801.

Chen, H., Shi, Y. J., and Wang, Y. Q. (2004a). "Fracture toughness properties of moment resistant column-beam connections Part I: elastic analysis." *International Journal of Steel Structures*, 4(1), pp. 1-7.

Chen, H., Shi, Y. J., and Wang, Y. Q. (2004b). "Fracture toughness properties of moment resistant column-beam connections Part II: inelastic analysis." *International Journal of Steel Structures*, 4(1), pp. 9-14.

Chi, W. M. and Deierlein, G. G. (2000). *Integration of analytical investigations on the fracture behavior of welded moment resisting connections*. Blume Center TR136, Stanford University, Stanford, CA.

Chi, W. M., Kanvinde, A. M., and Deierlein, G. G. (2006). "Prediction of ductile fracture in steel connections using SMCS criterion." *Journal of Structural Engineering*, 132(2), pp. 171-181.

GB/T 228 (2002). *Metallic materials - Tensile testing at ambient temperature*. Standards Press of China, Beijing (in Chinese).

GB/T 21143 (2007). *Metallic materials - Unified method of test for determination of quasistatic fracture toughness*. Standards Press of China, Beijing (in Chinese).

Hancock, J. W. and Mackenzie, A. C. (1976). "On the mechanics of ductile failure in high-strength steel subjected to multi-axial stress-states." *Journal of Mechanics and Physics of Solids*, 24(3), pp. 147-169.

Jones, S. L., Fry, G. T., and Engelhardt, M. D. (2002). "Experimental evaluation of cyclically loaded reduced beam section moment connections." *Journal of Structural Engineering*, 128(4), pp. 441-451.

Kanvinde, A. M. and Deierlein, G. G. (2004). *Micromechanical simulation of earthquake induced fracture in steel structures*. Blume Center TR145, Stanford University, Stanford, CA.

Kanvinde, A. M. and Deierlein, G. G. (2006). "Void growth model and stress modified critical strain model to predict ductile fracture in structural steels." *Journal of Structural Engineering*, 132(12), pp. 1907-1918.

Kanvinde, A. M. and Deierlein, G. G. (2007). "Finite-element simulation of ductile fracture in reduced section pull-plates using micromechanics-based fracture models." *Journal of Structural Engineering*, 133(5), pp. 656-664.

Kanvinde, A. M., Fell, B. V., Gomez, I. R., and Roberts, M. (2008). "Predicting fracture in structural fillet welds using traditional and micromechanical fracture models." *Engineering Structures*, 30(11), pp. 3325-3335.

Kanvinde, A. M., Gomez, I. R., Roberts, M., Fell, B. V., and Grondin, G. Y. (2009). "Strength and ductility of fillet welds with transverse root notch." *Journal of Constructional Steel Research*, 65(4), pp. 948-958.

Liao, F. F. and Wang, W. (2010). "Parameter calibrations of micromechanics-based fracture models of Q345 steel." *Sciencepaper Online*. <http://www.paper.edu.cn/index.php/default/releasepaper/content/201007-457>

Liu, Y. M., Zhang, Y. J., Chen, Y. Y., and Chen, Y. J. (2002). "Experimental research on fracture performance in weld heat-affect zone." *Chinese Quarterly of Mechanics*, 23(2), pp. 157-163 (in Chinese).

Matos, C. G. and Dodds, R. H. Jr. (2001). "Probabilistic modeling of weld fracture in steel frame connections part I: quasi-static loading." *Engineering Structures*, 23(8), pp. 1011-1030.

Matos, C. G. and Dodds, R. H. Jr. (2002) "Probabilistic modeling of weld fracture in steel frame connections part II: seismic loading." *Engineering Structures*, 24(6), pp. 687-705.

McClintock, F. A. (1968). "A criterion for ductile fracture by the growth of holes." *Journal of Applied Mechanics*, 35(2), pp. 363-371.

Rice, J. R. and Tracey, D. M. (1969). "On the ductile enlargement of voids in triaxial stress fields." *Journal of Mechanics and Physics of Solids*, 17(3), pp. 201-217.

Ricles, J. M., Fisher, J. W., Lu, L. W., and Kaufmann, E. J. (2002). "Development of improved welded moment connections for earthquake-resistant design." *Journal of Constructional Steel Research*, 58(5-8), pp. 565-604.

Righiniotis, T. D., Lancaster, E. R., and Hobbs, R. E. (2000). "Fracture strength of a moment resisting welded connection under combined loading Part I - Formulation." *Journal of Constructional Steel Research*, 56(1), pp. 17-30.

Righiniotis, T. D. and Hobbs, R. E. (2000). "Fracture strength of a moment resisting welded connection under combined loading Part II - Results." *Journal of Constructional Steel Research*, 56(1), pp. 31-45.

Stojadinović, B., Goel, S. C., Lee, K. H., and Choi, J. H. (2000). "Parametric tests on unreinforced steel moment connections." *Journal of Structural Engineering*, 126(1), pp. 40-49.

Uang, C. M., Yu, Q. S., Noel, S., and Gross, J. (2000). "Cyclic testing of steel moment connections rehabilitated with RBS or welded haunch." *Journal of Structural Engineering*, 126(1), pp. 57-68.

Wang, Y. Q., Zhou, H., Shi, Y. J., and Chen, H. (2010). "Fracture behavior analyses of welded beam-to-column connections based on elastic and inelastic fracture mechanics." *International Journal of Steel Structures*, 10(3), pp. 253-265.

Wu, Y. M. (2004). Research for mechanism of brittle fracture of structural steel and its engineering design method. *Ph.D. Dissertation*, Tsinghua University, Beijing, China (in Chinese).

Wu, Y. M., Wang, Y. Q., Shi, Y. J., and Jiang, J. J. (2004). "Effects of low temperature on properties of structural steels." *Journal of University of Science and Technology Beijing*, 11(5), pp. 442-448.